THE JOURNAL OF PHYSICAL CHEMISTRY C
A JOURNAL OF THE AMERICAN CHEMICAL SOCIETY

pubs.acs.org/JPCC

Article

Access and Capture of Layered Double Perovskite Polytypic Phase through High-Pressure Engineering

Published as part of The Journal of Physical Chemistry virtual special issue "Early-Career and Emerging Researchers in Physical Chemistry Volume 2".

Hanjun Yang, Wenwu Shi, Yasutaka Nagaoka, Zhenxian Liu, Ruipeng Li, and Ou Chen*

Cite This: *J. Phys. Chem. C* 2023, 127, 2407−2415

Read Online

ACCESS | Metrics & More | Article Recommendations | Supporting Information

ABSTRACT: Engineering halide perovskites through external pressure is as an effective means to tune the crystal structure, thus optoelectronic properties of the material. In this work, we studied the structural and optical property evolutions of $Cs_4M^{II}Bi_2Cl_{12}$ (M^{II}: Cd, $Cd_{0.8}Mn_{0.2}$, Mn) layered double perovskite (LDP) crystalline powders under high pressure. A novel polytypic phase transition was observed featuring lateral interlayer sliding of the Bi−M^{II}−Bi trilayer units, resulting in a new LDP-12R phase. Importantly, this high-pressure induced LDP-12R crystal phase can be preserved after complete decompression and captured at ambient conditions. Moreover, the LDP samples showed a pressure-dependent photoluminescence property. Our findings exemplified a new perovskite polytype that can be accessed and captured through high-pressure processing, advocating the uniqueness of LDP materials with soft and transformable crystal lattices.

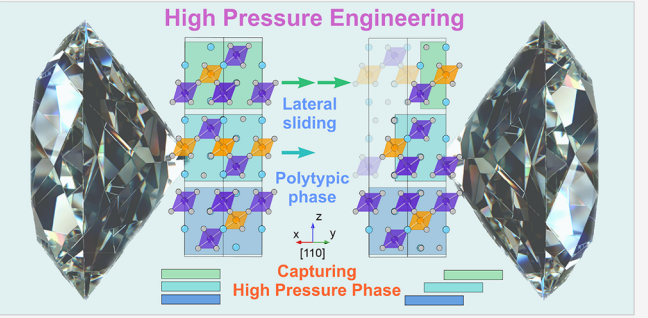

INTRODUCTION

Owing to the unique crystal structure and chemical composition, halide perovskites as a family of optoelectronic materials have gained unprecedented amount of research attention in the past decade.[1−7] Due to the structural complexity and tightly linked crystal structure−property relationship of perovskites and perovskite-derivative materials, controlling the crystal phase of such materials became an essential research topic for further advancing halide perovskites toward real-world technological applications.[8−10] With the goal of expanding optoelectronic properties as well as searching for low-toxicity alternatives to lead-based perovskites, lead-free perovskites have emerged as an increasingly important class of materials in recent years.[11−14] Metal cations in lead-free perovskites are often different in size and valence states than lead cations, thus resulting in crystal structures deviating from the conventional cubic perovskite lattice.[15−17] Therefore, the ever-expanding structure library of lead-free perovskites and perovskite derivatives are generally catalogued by the connectivity and symmetry of the MX_6 octahedral subunits in the crystalline lattices.[18,19] Such local structure versatility imparts soft and transformable features to the crystal, thus rendering high-pressure processing an effective means to modulate not only the crystal structure but also the structure-related optical/electronic behaviors of such materials.[20,21] For example, prior studies have proven that halide perovskites can undergo a phase transition under pressure from the high-symmetry phases (e.g., cubic $Fm\bar{3}m$ phase for $Cs_2AgBiCl_6$ and $Cs_2AgBiBr_6$) to the lower symmetry structures (e.g., $I4/m$ for $Cs_2AgBiCl_6$ at >5.6 GPa and $Cs_2AgBiBr_6$ at >4.5 GPa) driven by the deformation and tilting of the metal halide octahedra.[22−24] However, upon releasing the pressure, the crystal structure will typically revert to the original structures at ambient condition, thus greatly limiting the application value of the high-pressure technique. Some perovskite materials (e.g., $Cs_2NaBiCl_6$, etc.) are able to retain the properties observed at high pressure such as narrowed band gaps and pressure-induced emission after complete decompression.[22,25,26] However, those properties are typically retained through incomplete recrystallization from the amorphous high-pressure phase, while retainable high-pressure phases during simple compression−decompression processes have been less reported.[27,28]

Two-dimensional (2D) lead-free layered double perovskites (LDPs) have received extensive investigation as a potential optoelectronic material in photovoltaic, photodetector, and

Received: November 12, 2022
Revised: January 3, 2023
Published: January 25, 2023

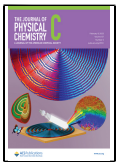

https://doi.org/10.1021/acs.jpcc.2c07970
J. Phys. Chem. C 2023, 127, 2407−2415

Scheme 1. (a) Schematic Illustration of the Relationship between the LDP-3C Phase and the LDP-12R Phase through Trilayer Lateral Sliding and (b) Unit Cell (UC) of the LDP-12R Phase with the Space Group $R\bar{3}m$

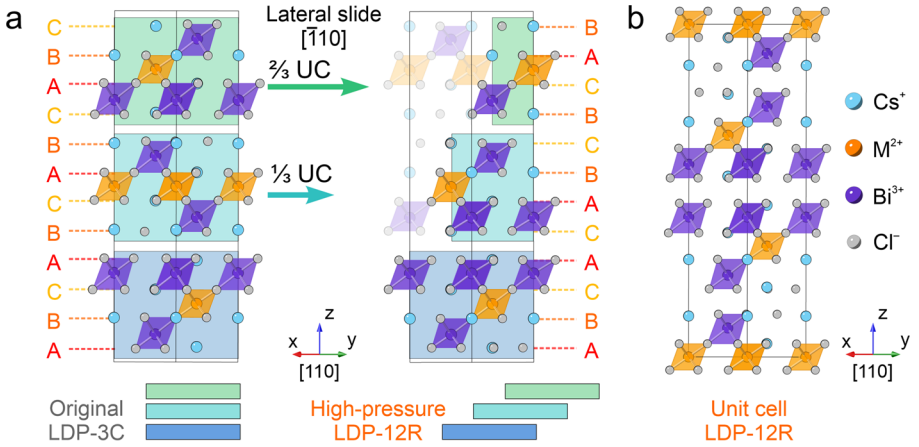

transparent conductor.[29−34] LDPs exhibit a general chemical formula of $A_4M^{II}M^{III}{}_2X_{12}$ (A = Cs; X = Cl and Br) that can be summarized as a product of replacing $[PbX_6]^{4-}$ octahedra in the conventional $APbX_3$ 3D lead-halide perovskites with $[M^{II}X_6]^{4-}$, $[M^{III}X_6]^{3-}$ octahedral units, and vacancies. As a result, within each (001) lattice plane of the LDP structure, the same types of metal halide octahedra (either $[M^{II}X_6]^{4-}$ or $[M^{III}X_6]^{3-}$ octahedra) are laterally assembled (Scheme 1a). Meanwhile, the LDP lattice exhibits a repeating pattern of $M^{III}-M^{II}-M^{III}$ trilayer units that are sandwiched by two vacancy layers (Scheme 1a).[35] The relatively weak inter-trilayer interaction makes LDPs prone to sliding along lateral directions, thus forming polytypic crystal motifs where the stacking sequence along the vertical direction alters while preserving other structural characteristics.[36] While such polytypic lattice motifs have been previously observed as low-population crystalline defects in lead-based perovskites,[37−39] to date, capture of the LDP materials with a pure polytypic crystalline phase has not been achieved to date.

Herein, we report a pressure-induced retainable phase transition of $Cs_4M^{II}Bi_2Cl_{12}$ (M^{II}: Cd, $Cd_{0.8}Mn_{0.2}$, or Mn) LDP powders. Upon applying pressure, the LDPs undergo a phase transition from the pristine phase to a new polytypic phase through lateral sliding of $Bi-M^{II}-Bi$ trilayer units along the [$\bar{1}$10] crystal direction (Scheme 1). Importantly, the resulting LDP high-pressure phase can be fully captured after complete decompression, demonstrating the retainability of this polytypic phase transition and the ambient stability of the resulting polytypic LDP materials. Moreover, we conducted *in situ* monitoring for the emission property evolution of the LDPs under pressure and discovered a pressure-induced localized defect-state emission. Our study not only presents the first example of harvesting a new LDP material with unique high-pressure polytypic phases but also sheds light on the crystal phase engineering of lead-free perovskites through clean and effective pressure engineering postsynthesis.

METHODS

Chemicals. Cesium chloride (CsCl, 99.9%), manganese chloride ($MnCl_2$, >99%) and cadmium chloride ($CdCl_2$, 99.99%) were obtained from Aldrich. Bismuth oxide (Bi_2O_3, 99.9%) was obtained from Acros Organics. Hydrochloric acid (37%, ACS plus), hexane, and ethanol were obtained from Fisher.

Synthesis of LDP Powders. The synthesis of $Cs_4M^{II}Bi_2Cl_{12}$ LDP (M^{II}: Cd or Mn) powder was adopted from the synthesis of $Cs_4MnSb_2Cl_{12}$ with modifications.[35] Bi_2O_3 (93.2 mg, 0.20 mmol), metal chloride ($CdCl_2$ (36.7 mg, 0.20 mmol), or $MnCl_2$ (25.2 mg, 0.20 mmol)) were dissolved in HCl (1 mL) separately. After complete dissolution, the Bi-containing solution was mixed with the metal chloride solution. CsCl (134.7 mg, 0.80 mmol) was dissolved in HCl (0.5 mL) and then added to the mixed precursors under stirring. White precipitates were formed upon the addition of CsCl. The formed $Cs_4M^{II}Bi_2Cl_{12}$ powder was centrifuged at 3000 rpm for 5 min and washed with 2% HCl and then ethanol, followed by washing with hexane for another two times. The product was centrifuged after washing each time. The obtained wet powder was dried at 70 °C for 1 h and then stored at ambient condition. For the synthesis of $Cs_4(Cd_{0.8}Mn_{0.2})Bi_2Cl_{12}$, a stoichiometric amount of a $CdCl_2$ and $MnCl_2$ ([Cd]:[Mn] = 8:2) mixture was added to the Bi solution and the rest of the synthesis follows the same procedure as for the $Cs_4M^{II}Bi_2Cl_{12}$ LDP (M^{II}: Cd or Mn) powder.

High-Pressure Experiments, Synchrotron-Based X-ray Scattering and PL Measurements. *In situ* wide-angle X-ray scattering (WAXS) measurements were performed at beamline 11-BM of National Synchrotron Light Source II (NSLS II) at Brookhaven National Laboratory (BNL). A diamond anvil cell (DAC) technique was used for all high-pressure experiments. A stainless gasket was preindented from 250 to ~70 μm, and a ~200 μm hole was drilled serving as the sample chamber for the powder LDP samples. Several ruby microcrystals were placed on top of the powder samples. The ruby photoluminescence (PL) (measured by Ocean Insight HR 2000+ spectrometer) excited by 532 nm laser (Spectra-physics) was used to monitor the pressure *in situ*. *In situ* PL was monitored by an Ocean Insight spectrometer USB2000+ with a 405 nm laser excitation. Raman spectra were measured *in situ* with a Witec Alpha 300 confocal Raman microscope using 532 nm laser excitation. The bulk modulus (K_0) was calculated with the second-order Birch−Murnaghan equation of states.

$$P(V) = \frac{3}{2}K_0\left[\left(\frac{V_0}{V}\right)^{7/3} - \left(\frac{V_0}{V}\right)^{5/3}\right]$$

https://doi.org/10.1021/acs.jpcc.2c07970
J. Phys. Chem. C 2023, 127, 2407−2415

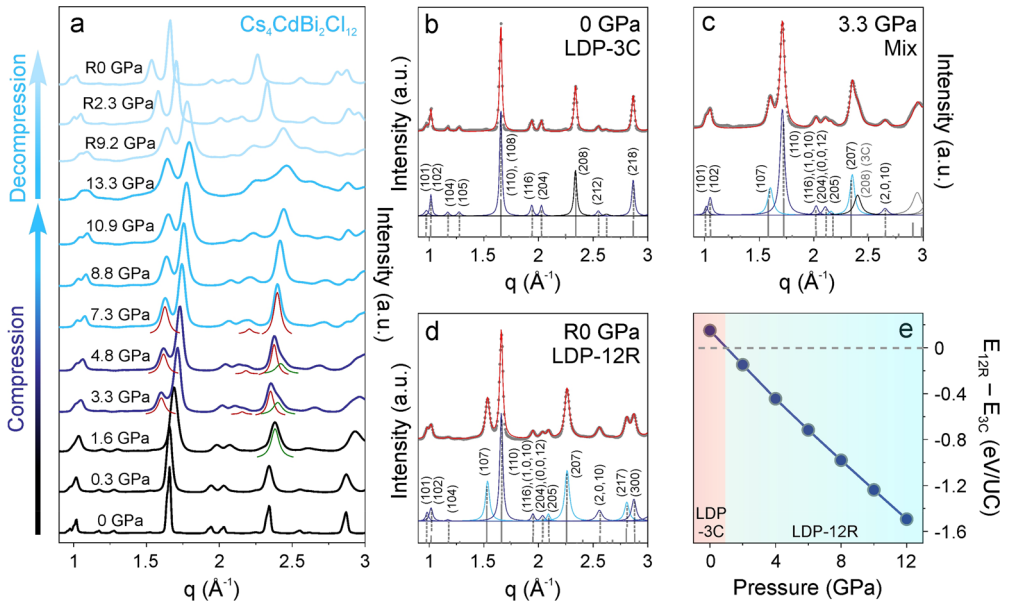

Figure 1. (a) WAXS patterns of $Cs_4CdBi_2Cl_{12}$ LDP at different pressures during the compression and decompression processes. Green and red lines represent the scattering peaks originated from the original LDP-3C and LDP-12R phases, respectively. (b–d) WAXS patterns of the LDP-3C phases at 0 GPa (b), the mixed phase at 3.3 GPa (c), and the LDP-12R phase after decompression (d). Simulated standard peak positions are represented by gray bars. Black, dark blue, and light blue lines represent scattering patterns originated from the original LDP-3C phase, both LDP-3C and LDP-12R phases, and the LDP-12R phase, respectively. (e) Calculated energy difference between the LDP-12R phase and LDP-3C phase of $Cs_4CdBi_2Cl_{12}$ LDP at different pressures.

P represents pressure, *V* represents the unit cell volume of the LDP sample, V_0 represents the unit cell volume of the LDP sample at ambient pressure, and K_0 represents bulk modulus at ambient pressure.

Density Functional Theory Calculation. All the simulations were based on the density functional theory (DFT) within the Vienna ab initio simulation package (VASP).[40,41] The exchange–correlation functional was described by the generalized gradient approximation (GGA), which was proposed by Perdew, Burke, and Ernzerhof (PBE),[42] and the cutoff energy used for the plane wave basis set extending was chosen to 520 eV. During the crystal relaxation, the lattice and atomic positions were fully relaxed until the residual force on each atom is less than 0.02 eV/Å. The Monkhorst–Pack grid 5 × 5 × 3 was adopted to integrate the first Brillouin zone. The crystal phase stability was determined by using energy difference (ΔE_f) between the LDP-3C and LDP-12R phases, which is defined as following equation:

$$\Delta E_f = E_{12R} - E_{3C}$$

where E_{3C} and E_{12R} are the total energy of $Cs_4CdBi_2Cl_{12}$ crystal structure with LDP-3C and LDP-12R phase, respectively.

RESULTS AND DISCUSSION

Crystalline powders of $Cs_4M^{II}Bi_2Cl_{12}$ (M^{II}: Cd, $Cd_{0.8}Mn_{0.2}$, or Mn) LDP (Trigonal phase, space group: $R\bar{3}m$, Scheme 1a) were synthesized using a reported precipitation method (see the Supporting Information for details).[35,43] At ambient condition, the stacking sequence of $CsCl_3$ sublattices along the [001] direction follows an *fcc*-type order (i.e., ABCABC..., Scheme 1a), denoted as the LDP-3C phase in this study. The synchrotron-based *in situ* wide-angle X-ray scattering (WAXS) technique was used to characterize the phase transition of LDP powders under high-pressure treatment using a diamond anvil cell.[21,44−46] Taking the $Cs_4CdBi_2Cl_{12}$ powder as an example, the original LDP-3C phase remained stable up to 1.6 GPa while all the WAXS peaks shifted to larger *q*-values (Figure 1a,b Figures S1 and S2, Tables S1−S6), corresponding to a gradual shrinkage of unit cell volume from 1849 to 1724 Å^3. A phase transition started when the pressure reached 3.3 GPa, which was indicated by the emergence of a set of new scattering features located at the *q*-values of 1.60, 2.15, and 2.35 Å^{-1} (Figure 1a,c). The phase transition completed at 7.3 GPa as indicated by the total disappearance of the initial (208) diffraction peak at 2.42 Å^{-1} (shoulder-like feature in the WAXS patterns at 3.3 and 4.8 GPa, Figure 1a). We assigned this newly formed high-pressure phase to an LDP polytypic structure as a result of the systematic sliding of the Bi–Cd–Bi octahedra units within the basal plane of the LDP crystal lattice (Scheme 1a,b). Specifically, during the phase transition, each Bi–Cd–Bi trilayer unit (together with four neighboring $CsCl_3$ layers) slides one-third of a unit cell along the $[\bar{1}10]$ direction (unit cell axes are maintained after phase transition). After phase transition, the stacking sequence of $CsCl_3$ sublattices along the [001] direction in a LDP unit cell changed from the initial *fcc*-type order (i.e., ABCA-BCAB-CABC) to a new polytypic order (i.e., ABCA-CABC-BCAB) with a 12-layer minimal repeating unit, thus denoted as the LDP-12R phase (Scheme 1b). While forming the new polytype of LDP-12R phase, both the characteristic Bi–Cd–Bi trilayer octahedra connectivity and the $R\bar{3}m$ space group of the original LDP structure were preserved (Scheme 1c). Upon further increasing pressure to the maximal value of 13.3 GPa, the unit cell volume of the LDP-12R phase continuously shrank to 1464 Å^3 without any additional phase transitions (Figure 1a).

Interestingly, the LDP-12R phase was maintained with gradually expanded unit cell volume during the decompression process and could be fully captured at ambient pressure (Figure 1b,d). The capture of this high-pressure phase

https://doi.org/10.1021/acs.jpcc.2c07970
J. Phys. Chem. C 2023, 127, 2407−2415

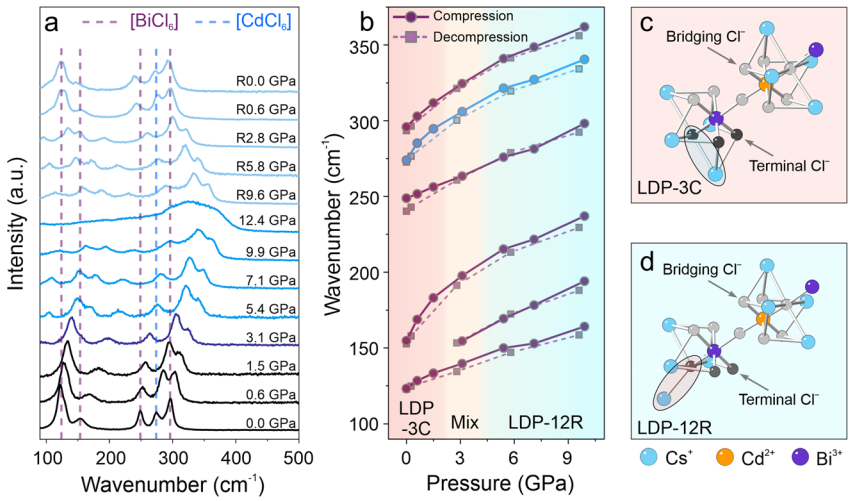

Figure 2. (a) Raman spectra of the $Cs_4CdBi_2Cl_{12}$ LDP powder at different pressures during the compression and decompression processes. Dashed lines mark the peak positions for the starting Raman spectrum of the sample at ambient pressure. (b) Raman peak evolutions of the $Cs_4CdBi_2Cl_{12}$ powder. $[BiCl_6]^{3-}$ related peaks are marked by purple lines and the $[CdCl_6]^{4-}$ related peak is marked by the blue line. Solid lines: compression process. Dashed lines: decompression process. (c, d) Local LDP structures to show the terminal Cl^- and bridging Cl^- anions in the LDP-3C and LDP-12R phases.

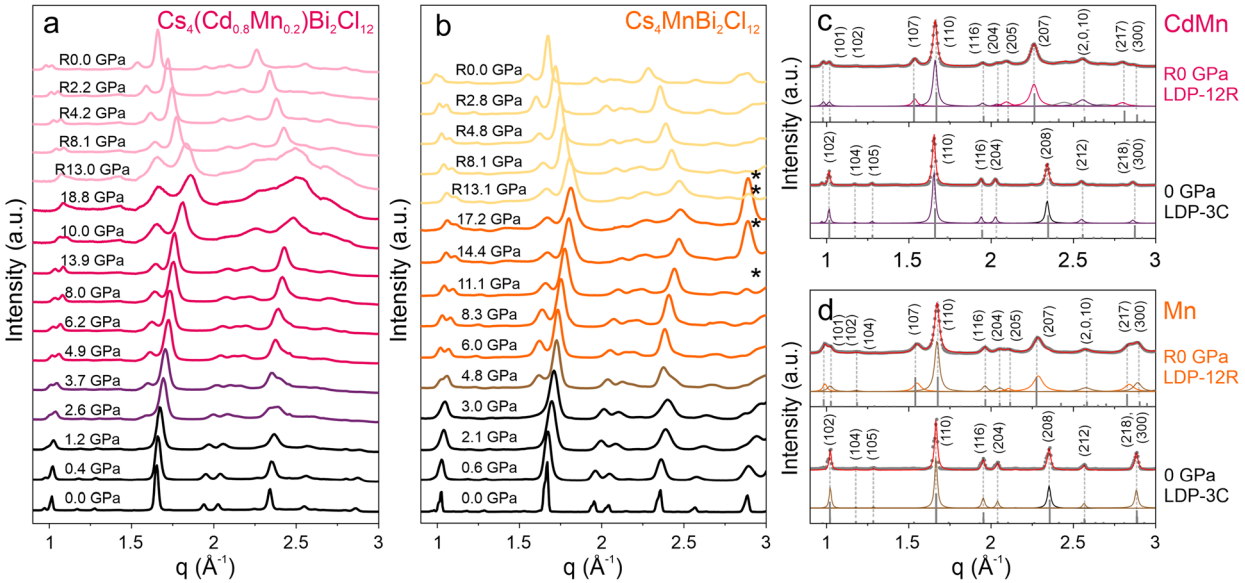

Figure 3. (a, b) WAXS evolutions of $Cs_4(Cd_{0.8}Mn_{0.2})Bi_2Cl_{12}$ (a) and $Cs_4MnBi_2Cl_{12}$ (b) LDP powder samples during the pressure cycle. (c, d) WAXS patterns of the LDP-3C phase (bottom) and LDP-12R phase (top) of the $Cs_4(Cd_{0.8}Mn_{0.2})Bi_2Cl_{12}$ (c) and $Cs_4MnBi_2Cl_{12}$ (d) LDP samples before compression and after complete decompression. Simulated standard peak positions are represented by gray bars. Black, purple, and pink lines in (c) represent scattering patterns originated from the original LDP-3C phase, both LDP-3C and LDP-12R phases, and the LDP-12R phase, respectively. Black, yellow, and orange lines in (d) represent scattering patterns originated from the original LDP-3C phase, both LDP-3C and LDP-12R phases, and the LDP-12R phase, respectively.

suggested a retainability of the resulting LDP-12R crystal structure, which was further confirmed by lattice energy calculations based on density functional theory (DFT). The calculation results showed that while the LDP-12R phase exhibited a slightly higher energy (+0.15 eV/unit cell) than the LDP-3C phase at ambient pressure, it became the energetically favored structure at elevated pressure (>1 GPa, Figure 1e). Such a small lattice energy difference (i.e., 0.15 eV/unit cell) between the two phases, i.e., LDP-3C and LDP-12R phases, agreed well with our experimental observations that (1) the phase transition took place at relatively low pressure, and (2) the high-pressure LDP-12R phase could be captured at ambient pressure. Both the experimental results and DFT calculations proved that external pressure processing could be used as an effective means to tune the phase of LDP materials.

The $Cs_4CdBi_2Cl_{12}$ LDP-3C-to-12R phase transition was further studied through Raman spectroscopy measurements. The majority of the Raman peaks were assigned to the vibrational modes of $[BiCl_6]^{3-}$: the peaks at 295 and 249 cm^{-1} could be assigned to the A_{1g} symmetric stretching and E_g asymmetric stretching, respectively. The two peaks at 123 and 155 cm^{-1} were assigned to the scissoring modes of $[BiCl_6]^{3-}$. Lastly, the peak at 275 cm^{-1} was assigned to the A_{1g} stretching mode of $[CdCl_6]^{4-}$ octahedra.[47−50] All Raman peaks shifted to larger wavenumbers with increasing pressure, corresponding to a universal contraction of the chemical bonds. All Raman peaks

https://doi.org/10.1021/acs.jpcc.2c07970
J. Phys. Chem. C 2023, 127, 2407−2415

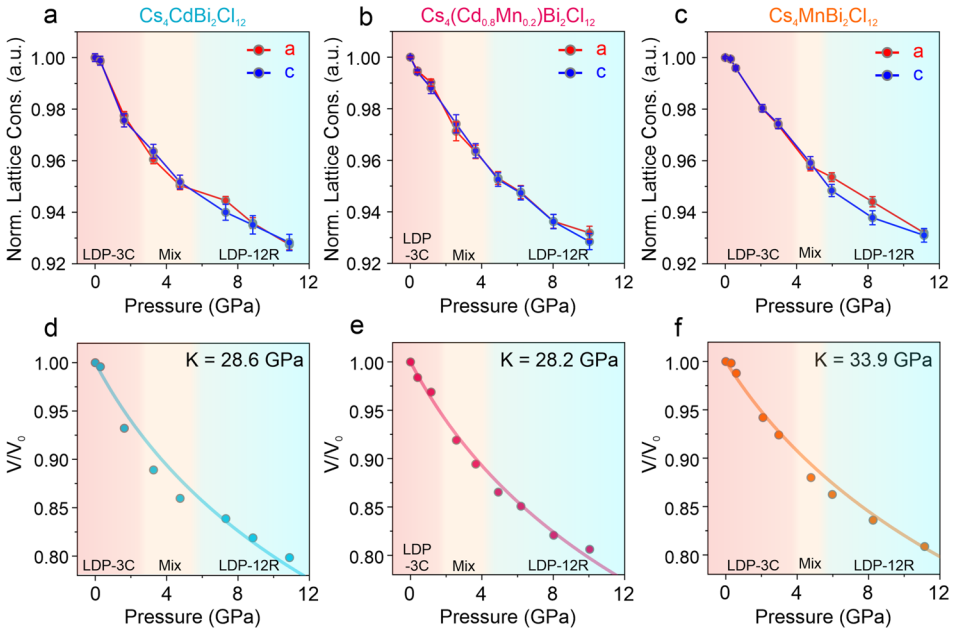

Figure 4. (a–c) Normalized lattice constant evolutions of $Cs_4CdBi_2Cl_{12}$ (a), $Cs_4(Cd_{0.8}Mn_{0.2})Bi_2Cl_{12}$ (b), and $Cs_4MnBi_2Cl_{12}$ (c) during the compression process. The background color represents different phases determined based on the WAXS data analyses. (d–f) Bulk moduli of $Cs_4CdBi_2Cl_{12}$ (d), $Cs_4(Cd_{0.8}Mn_{0.2})Bi_2Cl_{12}$ (e), and $Cs_4MnBi_2Cl_{12}$ (f) LDP powders, obtained by the second-order Birch–Murnaghan equation of state fitting.

became broader with increasing pressure until they became indistinguishable at 12.4 GPa, reflecting an increase in structural disorder because of the applied pressure (Figure 2a). The T_{2g} scissoring mode of $[BiCl_6]^{3-}$ further split at 3.1 GPa, resulting in an additional peak at 155 cm^{-1} caused by the distortion of the $[BiCl_6]^{3-}$ octahedral at high pressure.[51] Upon complete release of pressure, the A_{1g} mode of $[BiCl_6]^{3-}$ octahedra irreversibly shifted from 296 to 293 cm^{-1}, and more obviously, the E_g mode shifted from 249 to 240 cm^{-1} (Figure 2b). The irreversible shifts of the Raman peaks are attributed to the local structure change of the terminal Cl^- anions in the $[BiCl_6]^{3-}$ octahedra (Figure 2c, d). Specifically, each $[BiCl_6]^{3-}$ octahedron is composed of three terminal Cl^- anions and three bridging Cl^- anions (Figure S3). The three terminal ones are located at the top and bottom atomic layers of the Bi–Cd–Bi trilayer units and bonded to both Cs^+ within their trilayer units and the Cs^+ in the adjacent trilayer unit that slides during the phase transition (Figure 2c,d and Figure S3). In contrast, the three bridging Cl^- anions are embedded inside each trilayer unit and thus not bonded to any ions in the adjacent trilayers (Figure 2c,d). During the LDP-3C-to-12R phase transition, while the local coordination environment of the bridging Cl^- anions was preserved, the terminal Cl^- anions underwent a slide relative to the adjacent $CsCl_3$ layer and thus one Cs^+ cation moved to the position opposite to the Bi^{3+} cation (Figure 2c,d). Such local structure variation affects the symmetry as well as Bi–Cl bond strength, thus influencing the energy and intensity of the vibration modes of the Bi–Cl bonds, leading to the observed red shifts of the Raman peaks for the $[BiCl_6]^{3-}$ octahedra. In comparison, the $[CdCl_6]^{4-}$ octahedral units contain only the bridging Cl^- anions with a nearly unchanged local coordination environment; thus the related Raman peak stayed almost unchanged after the high-pressure cycle (Figure 2a,b). Overall, the discrepancy between the Bi-related and Cd-related Raman shifts supported the observed polytypic LDP-3C-to-12R phase transformation through lateral inter-trilayer sliding as shown in Scheme 1.

The LDP-3C-to-12R phase transition was also observed for the alloyed $Cs_4(Cd_{0.8}Mn_{0.2})Bi_2Cl_{12}$ and the $Cs_4MnBi_2Cl_{12}$ LDP powder samples (Figure 3, Figures S4–S7, Tables S7–S18). The transition to LDP-12R phase for $Cs_4(Cd_{0.8}Mn_{0.2})Bi_2Cl_{12}$ and $Cs_4MnBi_2Cl_{12}$ LDP samples occurred at the pressure ranges of 2.6–4.9 and 4.8–6.0 GPa, respectively (Figure 3a,b). Similar to the $Cs_4CdBi_2Cl_{12}$ LDP sample, the high-pressure LDP-12R phases could be fully captured at ambient condition for both samples after decompression (Figure 3c,d). Prior reports showed that the $Cs_4MnBi_2Cl_{12}$ LDP single crystal might go through a phase transition from the hexagonal $R\bar{3}m$ phase to a cubic $Fd\bar{3}m$ phase at ~2 GPa, followed by a second transition to the orthorhombic *Imma* phase at ~9 GPa.[51] However, none of the high-pressure structures was observed in our experiments, suggesting that the pressure-induced phase transition pathway was altered depending on the initial form of the LDP materials. In addition, considerable deviatoric pressure may also contribute to the retaining of the LDP-12R phase, as it has proven to show influence on the high-pressure phase transition and morphology control of nanocrystalline materials.[52,53]

The evolution of the lattice constants of the three LDP powder samples during compression are summarized in Figure 4. For all LDP samples tested here, negligible anisotropies in the compressibility were observed throughout the process (Figure 4a–c), in contrast to other inorganic layered perovskites such as $A_3Bi_2Br_9$, which commonly show a higher axial compressibility than the equatorial one.[54] The bulk moduli were extracted to be 28.6, 28.2, and 33.9 GPa for the $Cs_4CdBi_2Cl_{12}$, $Cs_4(Cd_{0.8}Mn_{0.2})Bi_2Cl_{12}$ and $Cs_4MnBi_2Cl_{12}$ samples, respectively (Figure 4d–f). These values are noticeably lower than that of the $CsPbCl_3$ perovskite powder (i.e., 45.6 GPa),[55] in good accordance with the soft and prone-to-transformation nature of the LDPs under high pressure.

https://doi.org/10.1021/acs.jpcc.2c07970
J. Phys. Chem. C 2023, 127, 2407–2415

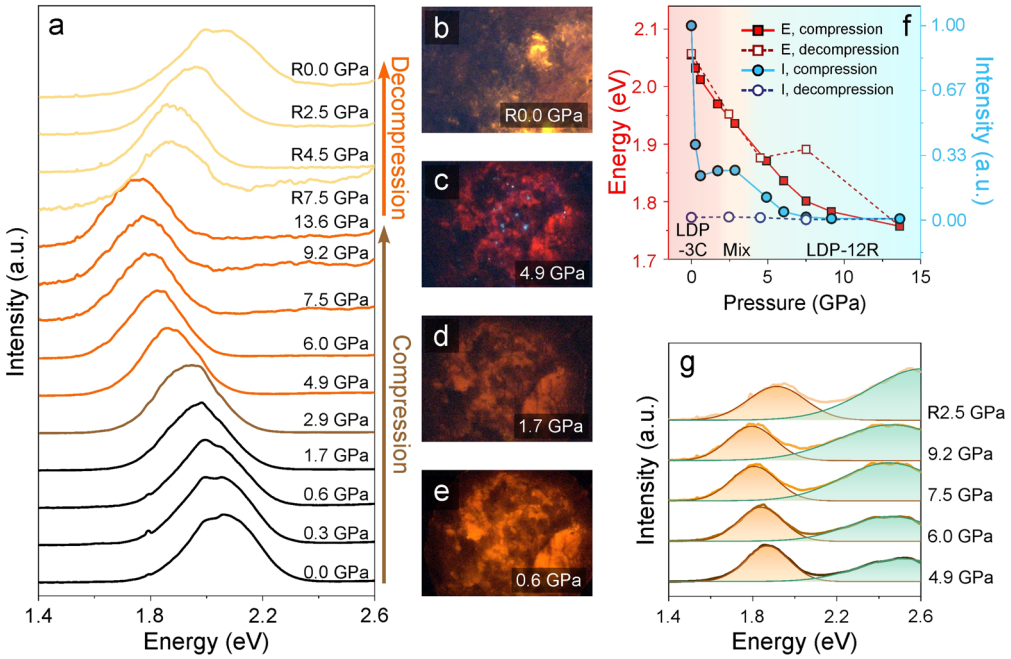

Figure 5. (a) Normalized PL spectra of the $Cs_4MnBi_2Cl_{12}$ LDP powder at different pressures. (b–e) Optical microscope images of the $Cs_4MnBi_2Cl_{12}$ LDP powder at different pressures under UV excitation. (f) Evolution of the PL peak energy (red squares) and intensity (blue circles) during the pressure cycle. (g) PL spectra acquired at the green emitting regions. All spectra are normalized based on the Mn PL peak around 1.8–1.9 eV.

Emission property evolutions of the LDP samples under pressure were monitored by *in situ* PL spectroscopy. The PL peak of $Cs_4MnBi_2Cl_{12}$ LDP powder red-shifted gradually from 2.06 to 1.76 eV upon compression from ambient pressure to 13.6 GPa (Figure 5a–e). The pressure-induced PL peak energy decrease is similar to that for other Mn-containing halide perovskite systems, showing a decreased energy gap between the $^4T_1$ and $^6A_1$ electronic states of Mn^{2+} under pressure as a result of strengthened crystal field splitting.[56,57] The PL intensity quickly decreased down to 23% of the initial value when the pressure only reached 0.6 GPa, followed by a brief plateau to 2.9 GPa and then a gradual decrease between 2.9 and 6.0 GPa (Figure 5f). Considering that the LDP-3C-to-12R phase transition takes place between 3.0 and 6.0 GPa, we assign the initial quick decrease of the PL intensity to the formation of nonradiative surface and crystalline defects.[56] The following slow PL intensity decrease (2.9–6.0 GPa) can be explained by the gradual phase transition to the LDP-12R phase with interlayer sliding. The deviatoric stress may also contribute to the decreased emission intensity.[22] Upon releasing the pressure, the PL peak energy completely reverted to 2.06 eV, whereas the PL intensity remained significantly lower than the initial PL intensity of the sample before press (Figure 5f, Figure S8). Similar PL evolution under elevated pressure was observed for the $Cs_4(Cd_{0.8}Mn_{0.2})Bi_2Cl_{12}$ LDP sample, despite the large difference in their PL quantum yields (1.2% for $Cs_4MnBi_2Cl_{12}$, 46% for $Cs_4(Cd_{0.8}Mn_{0.2})Bi_2Cl_{12}$)[35] which possessed a much weaker Mn–Mn coupling effect than the $Cs_4MnBi_2Cl_{12}$ LDP (Figure S9), suggesting that the strength of Mn–Mn coupling was not responsible for PL evolution behavior of the LDP powders under the pressure processing.[35] Interestingly, broad PL peaks centered at 2.44–2.61 and 2.23–2.35 eV for the $Cs_4MnBi_2Cl_{12}$ and $Cs_4(Cd_{0.8}Mn_{0.2})Bi_2Cl_{12}$ samples, respectively, emerged in some local areas when the pressure reached 4.9 and 4.2 GPa, respectively (Figure 5c,g, Figure S9c). We tentatively assign this green emission to the pressure-induced defect states, which compete with the Mn^{2+} ion emission center for the energy transfer process from the neighboring $[BiCl_6]^{3-}$ frameworks. Considering the green emission emerges in the pressure range of phase transition, it may originate from the defects caused by the lateral slide of the Bi–M^{II}–Bi octahedral trilayer units and the corresponding $[BiCl_6]^{3-}$ local environment change as we have discussed above. Similar broad green emission features were also observed for the $Cs_4CdBi_2Cl_{12}$ LDP sample under pressure (Figure S10), as well as in a previous report on $Cs_2AgBiCl_6$ perovskite under high pressure,[23] suggesting that the origin of the green emission is from the Birelated motifs rather than Mn-related ones. Further research is still needed to identify the radiative mechanism of these observed green emission features.

CONCLUSION

In summary, we report a pressure-induced polytypic phase transition from the initial LDP-3C phase to a new LDP-12R phase for the $Cs_4M^{II}Bi_2Cl_{12}$ LDP (M^{II}: Cd, $Cd_{0.8}Mn_{0.2}$, or Mn) powder samples as a result of lateral sliding of the Bi–M^{II}–Bi octahedral trilayer units. Importantly, this newly transformed LDP-12R phase can be fully captured at ambient conditions after complete release of pressure, suggesting a metastability of the obtained LDP-12R phase. Optically, the samples with an LDP-12R phase showed decreased PL efficiency and defect-induced emission at elevated pressure. The retainability of the high-pressure phase transition provides a novel method of manipulating crystal structures and thus optoelectronic properties of lead-free halide perovskite materials by using facile high-pressure engineering.

https://doi.org/10.1021/acs.jpcc.2c07970
J. Phys. Chem. C 2023, 127, 2407–2415

■ ASSOCIATED CONTENT

Supporting Information

The Supporting Information is available free of charge at https://pubs.acs.org/doi/10.1021/acs.jpcc.2c07970.

Schematic illustration of crystal structures, WAXS patterns and fitting data, Evolution of the lattice constants, additional photoluminescence data (PDF)

■ AUTHOR INFORMATION

Corresponding Author

Ou Chen − *Department of Chemistry, Brown University, Providence, Rhode Island 02912, United States;* orcid.org/0000-0003-0551-090X; Email: ouchen@brown.edu

Authors

Hanjun Yang − *Department of Chemistry, Brown University, Providence, Rhode Island 02912, United States;* orcid.org/0000-0002-6856-6559

Wenwu Shi − *Department of Chemistry, Brown University, Providence, Rhode Island 02912, United States*

Yasutaka Nagaoka − *Department of Chemistry, Brown University, Providence, Rhode Island 02912, United States;* orcid.org/0000-0001-8612-2612

Zhenxian Liu − *Department of Physics, University of Illinois at Chicago, Chicago, Illinois 60607, United States*

Ruipeng Li − *National Synchrotron Light Source II, Brookhaven National Laboratory, Upton, New York 11973, United States*

Complete contact information is available at: https://pubs.acs.org/10.1021/acs.jpcc.2c07970

Author Contributions

H.Y. and O.C. conceptualized the project. H.Y. conducted sample preparation. H.Y., Y.N., Z.L., and R.L. conducted the high-pressure WAXS measurements. H.Y. conducted the high-pressure PL and Raman measurements. W.S. conducted the DFT calculations. O.C. supervised the project. The manuscript was written through contributions of all authors. All authors have given approval to the final version of the manuscript.

Notes

The authors declare no competing financial interest.

■ ACKNOWLEDGMENTS

O.C. acknowledges the support from Alfred P. Sloan Foundation through Sloan Research Fellowship Award program and 3M Foundation through the Non-Tenured Faculty Award program. This research used the CMS beamline of the of the National Synchrotron Light Source II, a U.S. Department of Energy (DOE), Office of Science User Facility, operated for the DOE, Office of Science, by Brookhaven National Laboratory under Contract DE-SC0012704. Use of the 22-IR-1 beamline of NSLS-II is supported by COMPRES, the Consortium for Materials Properties Research in Earth Sciences, under NSF Cooperative Agreement EAR 1606856 and CDAC (DE-NA0003975).

■ REFERENCES

(1) Kojima, A.; Teshima, K.; Shirai, Y.; Miyasaka, T. Organometal Halide Perovskites as Visible-Light Sensitizers for Photovoltaic Cells. *J. Am. Chem. Soc.* **2009**, *131* (17), 6050−6051.

(2) Lee, M. M.; Teuscher, J.; Miyasaka, T.; Murakami, T. N.; Snaith, H. J. Efficient Hybrid Solar Cells Based on Meso-Superstructured Organometal Halide Perovskites. *Science* **2012**, *338* (6107), 643−647.

(3) Tan, Z.-K.; Moghaddam, R. S.; Lai, M. L.; Docampo, P.; Higler, R.; Deschler, F.; Price, M.; Sadhanala, A.; Pazos, L. M.; Credgington, D.; et al. Bright light-emitting diodes based on organometal halide perovskite. *Nat. Nanotechnol.* **2014**, *9* (9), 687−692.

(4) Protesescu, L.; Yakunin, S.; Bodnarchuk, M. I.; Krieg, F.; Caputo, R.; Hendon, C. H.; Yang, R. X.; Walsh, A.; Kovalenko, M. V. Nanocrystals of Cesium Lead Halide Perovskites ($CsPbX_3$, X = Cl, Br, and I): Novel Optoelectronic Materials Showing Bright Emission with Wide Color Gamut. *Nano Lett.* **2015**, *15* (6), 3692−3696.

(5) Hills-Kimball, K.; Yang, H.; Cai, T.; Wang, J.; Chen, O. Recent Advances in Ligand Design and Engineering in Lead Halide Perovskite Nanocrystals. *Adv. Sci.* **2021**, *8* (12), 2100214.

(6) Kim, J. Y.; Lee, J.-W.; Jung, H. S.; Shin, H.; Park, N.-G. High-Efficiency Perovskite Solar Cells. *Chem. Rev.* **2020**, *120* (15), 7867−7918.

(7) Zhang, F.; Zhong, H.; Chen, C.; Wu, X.-g.; Hu, X.; Huang, H.; Han, J.; Zou, B.; Dong, Y. Brightly Luminescent and Color-Tunable Colloidal $CH_3NH_3PbX_3$ (X = Br, I, Cl) Quantum Dots: Potential Alternatives for Display Technology. *ACS Nano* **2015**, *9* (4), 4533−4542.

(8) Swarnkar, A.; Marshall, A. R.; Sanehira, E. M.; Chernomordik, B. D.; Moore, D. T.; Christians, J. A.; Chakrabarti, T.; Luther, J. M. Quantum dot-induced phase stabilization of α-$CsPbI_3$ perovskite for high-efficiency photovoltaics. *Science* **2016**, *354* (6308), 92.

(9) Straus, D. B.; Guo, S.; Cava, R. J. Kinetically Stable Single Crystals of Perovskite-Phase $CsPbI_3$. *J. Am. Chem. Soc.* **2019**, *141* (29), 11435−11439.

(10) Liu, Y.; Akin, S.; Hinderhofer, A.; Eickemeyer, F. T.; Zhu, H.; Seo, J.-Y.; Zhang, J.; Schreiber, F.; Zhang, H.; Zakeeruddin, S. M.; et al. Stabilization of Highly Efficient and Stable Phase-Pure $FAPbI_3$ Perovskite Solar Cells by Molecularly Tailored 2D-Overlayers. *Angew. Chem., Int. Ed.* **2020**, *59* (36), 15688−15694.

(11) Hao, F.; Stoumpos, C. C.; Cao, D. H.; Chang, R. P. H.; Kanatzidis, M. G. Lead-free solid-state organic-inorganic halide perovskite solar cells. *Nat. Photonics* **2014**, *8* (6), 489−494.

(12) Leng, M.; Chen, Z.; Yang, Y.; Li, Z.; Zeng, K.; Li, K.; Niu, G.; He, Y.; Zhou, Q.; Tang, J. Lead-Free, Blue Emitting Bismuth Halide Perovskite Quantum Dots. *Angew. Chem., Int. Ed.* **2016**, *55* (48), 15012−15016.

(13) Feng, H.-J.; Deng, W.; Yang, K.; Huang, J.; Zeng, X. C. Double Perovskite Cs_2BBiX_6 (B = Ag, Cu; X = Br, Cl)/TiO_2 Heterojunction: An Efficient Pb-Free Perovskite Interface for Charge Extraction. *J. Phys. Chem. C* **2017**, *121* (8), 4471−4480.

(14) Liu, Y.; Nag, A.; Manna, L.; Xia, Z. Lead-Free Double Perovskite $Cs_2AgInCl_6$. *Angew. Chem., Int. Ed.* **2021**, *60* (21), 11592−11603.

(15) Yang, H.; Cai, T.; Liu, E.; Hills-Kimball, K.; Gao, J.; Chen, O. Synthesis and Transformation of Zero-Dimensional Cs_3BiX_6 (X = Cl, Br) Perovskite-Analogue Nanocrystals. *Nano Res.* **2020**, *13* (1), 282−291.

(16) Park, B.-W.; Philippe, B.; Zhang, X.; Rensmo, H.; Boschloo, G.; Johansson, E. M. J. Bismuth Based Hybrid Perovskites $A_3Bi_2I_9$ (A: Methylammonium or Cesium) for Solar Cell Application. *Adv. Mater.* **2015**, *27* (43), 6806−6813.

(17) Akkerman, Q. A.; Park, S.; Radicchi, E.; Nunzi, F.; Mosconi, E.; De Angelis, F.; Brescia, R.; Rastogi, P.; Prato, M.; Manna, L. Nearly Monodisperse Insulator Cs_4PbX_6 (X = Cl, Br, I) Nanocrystals, Their Mixed Halide Compositions, and Their Transformation into $CsPbX_3$ Nanocrystals. *Nano Lett.* **2017**, *17* (3), 1924−1930.

(18) Saidaminov, M. I.; Mohammed, O. F.; Bakr, O. M. Low-Dimensional-Networked Metal Halide Perovskites: The Next Big Thing. *ACS Energy Lett.* **2017**, *2* (4), 889−896.

(19) Creutz, S. E.; Liu, H.; Kaiser, M. E.; Li, X.; Gamelin, D. R. Structural Diversity in Cesium-Bismuth-Halide Nanocrystals. *Chem. Mater.* **2019**, *31* (13), 4685−4697.

(20) Zhu, H.; Cai, T.; Que, M.; Song, J.-P.; Rubenstein, B. M.; Wang, Z.; Chen, O. Pressure-Induced Phase Transformation and Band-Gap Engineering of Formamidinium Lead Iodide Perovskite Nanocrystals. *J. Phys. Chem. Lett.* **2018**, *9* (15), 4199−4205.
(21) Nagaoka, Y.; Hills-Kimball, K.; Tan, R.; Li, R.; Wang, Z.; Chen, O. Nanocube Superlattices of Cesium Lead Bromide Perovskites and Pressure-Induced Phase Transformations at Atomic and Mesoscale Levels. *Adv. Mater.* **2017**, *29* (18), 1606666.
(22) Zhang, L.; Liu, Z.; Sun, X.; Niu, G.; Jiang, J.; Fang, Y.; Duan, D.; Wang, K.; Sui, L.; Yuan, K.; et al. Retainable Bandgap Narrowing and Enhanced Photoluminescence in Mn-Doped and Undoped $Cs_2NaBiCl_6$ Double Perovskites by Pressure Engineering. *Adv. Opt. Mater.* **2022**, *10* (2), 2101892.
(23) Zhang, L.; Fang, Y.; Sui, L.; Yan, J.; Wang, K.; Yuan, K.; Mao, W. L.; Zou, B. Tuning Emission and Electron-Phonon Coupling in Lead-Free Halide Double Perovskite $Cs_2AgBiCl_6$ under Pressure. *ACS Energy Lett.* **2019**, *4* (12), 2975−2982.
(24) Li, Q.; Wang, Y.; Pan, W.; Yang, W.; Zou, B.; Tang, J.; Quan, Z. High-Pressure Band-Gap Engineering in Lead-Free $Cs_2AgBiBr_6$ Double Perovskite. *Angew. Chem., Int. Ed.* **2017**, *56* (50), 15969−15973.
(25) Zhao, D.; Xiao, G.; Liu, Z.; Sui, L.; Yuan, K.; Ma, Z.; Zou, B. Harvesting Cool Daylight in Hybrid Organic-Inorganic Halides Microtubules through the Reservation of Pressure-Induced Emission. *Adv. Mater.* **2021**, *33* (31), 2100323.
(26) Fu, R.; Zhao, W.; Wang, L.; Ma, Z.; Xiao, G.; Zou, B. Pressure-Induced Emission toward Harvesting Cold White Light from Warm White Light. *Angew. Chem., Int. Ed.* **2021**, *60* (18), 10082−10088.
(27) Ke, F.; Wang, C.; Jia, C.; Wolf, N. R.; Yan, J.; Niu, S.; Devereaux, T. P.; Karunadasa, H. I.; Mao, W. L.; Lin, Y. Preserving a robust $CsPbI_3$ perovskite phase via pressure-directed octahedral tilt. *Nat. Commun.* **2021**, *12* (1), 461.
(28) Liu, G.; Gong, J.; Kong, L.; Schaller, R. D.; Hu, Q.; Liu, Z.; Yan, S.; Yang, W.; Stoumpos, C. C.; Kanatzidis, M. G.; et al. Isothermal pressure-derived metastable states in 2D hybrid perovskites showing enduring bandgap narrowing. *Proc. Natl. Acad. Sci. U. S. A.* **2018**, *115* (32), 8076−8081.
(29) Tang, G.; Xiao, Z.; Hosono, H.; Kamiya, T.; Fang, D.; Hong, J. Layered Halide Double Perovskites $Cs_{3+n}M(II)_nSb_2X_{9+3n}$ (M = Sn, Ge) for Photovoltaic Applications. *J. Phys. Chem. Lett.* **2018**, *9* (1), 43−48.
(30) Vargas, B.; Ramos, E.; Pérez-Gutiérrez, E.; Alonso, J. C.; Solis-Ibarra, D. A Direct Bandgap Copper-Antimony Halide Perovskite. *J. Am. Chem. Soc.* **2017**, *139* (27), 9116−9119.
(31) Cai, T.; Shi, W.; Hwang, S.; Kobbekaduwa, K.; Nagaoka, Y.; Yang, H.; Hills-Kimball, K.; Zhu, H.; Wang, J.; Wang, Z.; et al. Lead-Free $Cs_4CuSb_2Cl_{12}$ Layered Double Perovskite Nanocrystals. *J. Am. Chem. Soc.* **2020**, *142* (27), 11927−11936.
(32) Cai, T.; Shi, W.; Gosztola, D. J.; Kobbekaduwa, K.; Yang, H.; Jin, N.; Nagaoka, Y.; Dube, L.; Schneider, J.; Hwang, S.; et al. Colloidal Synthesis and Charge Carrier Dynamics of $Cs_4Cd_{1-x}Cu_xSb_2Cl_{12}$ ($0 \le x \le 1$) Layered Double Perovskite Nanocrystals. *Matter* **2021**, *4* (9), 2936−2952.
(33) Xu, J.; Liu, J.-B.; Wang, J.; Liu, B.-X.; Huang, B. Prediction of Novel p-Type Transparent Conductors in Layered Double Perovskites: A First-Principles Study. *Adv. Funct. Mater.* **2018**, *28* (26), 1800332.
(34) Cai, T.; Dube, L.; Saghy, P.; Yang, H.; Chen, O. Progress in all-inorganic heterometallic halide layered double perovskites. *Trends Chem.* **2023**, *5*, 29.
(35) Yang, H.; Shi, W.; Cai, T.; Hills-Kimball, K.; Liu, Z.; Dube, L.; Chen, O. Synthesis of Lead-Free Cs_4 $(Cd_{1-x}Mn_x)$ Bi_2Cl_{12} ($0 \le x \le 1$) Layered Double Perovskite Nanocrystals with Controlled Mn-Mn Coupling Interaction. *Nanoscale* **2020**, *12* (45), 23191−23199.
(36) Guo, S.; Bu, K.; Li, J.; Hu, Q.; Luo, H.; He, Y.; Wu, Y.; Zhang, D.; Zhao, Y.; Yang, W.; et al. Enhanced Photocurrent of All-Inorganic Two-Dimensional Perovskite $Cs_2PbI_2Cl_2$ via Pressure-Regulated Excitonic Features. *J. Am. Chem. Soc.* **2021**, *143* (6), 2545−2551.
(37) Park, J.-S.; Li, Z.; Wilson, J. N.; Yin, W.-J.; Walsh, A. Hexagonal Stacking Faults Act as Hole-Blocking Layers in Lead Halide Perovskites. *ACS Energy Lett.* **2020**, *5* (7), 2231−2233.
(38) Rothmann, M. U.; Kim, J. S.; Borchert, J.; Lohmann, K. B.; O'Leary, C. M.; Sheader, A. A.; Clark, L.; Snaith, H. J.; Johnston, M. B.; Nellist, P. D. et al, Atomic-scale microstructure of metal halide perovskite. *Science* **2020**, *370* (6516), No. eabb5940.
(39) Nan, Z.-A.; Chen, L.; Liu, Q.; Wang, S.-H.; Chen, Z.-X.; Kang, S.-Y.; Ji, J.-B.; Tan, Y.-Y.; Hui, Y.; Yan, J.-W.; et al. Revealing phase evolution mechanism for stabilizing formamidinium-based lead halide perovskites by a key intermediate phase. *Chem.* **2021**, *7* (9), 2513−2526.
(40) Kresse, G.; Furthmüller, J. Efficient iterative schemes for ab initio total-energy calculations using a plane-wave basis set. *Phys. Rev. B* **1996**, *54* (16), 11169−11186.
(41) Kresse, G.; Joubert, D. From ultrasoft pseudopotentials to the projector augmented-wave method. *Phys. Rev. B* **1999**, *59* (3), 1758−1775.
(42) Perdew, J. P.; Burke, K.; Ernzerhof, M. Generalized gradient approximation made simple. *Phys. Rev. Lett.* **1996**, *77* (18), 3865.
(43) Vargas, B.; Torres-Cadena, R.; Rodríguez-Hernández, J.; Gembicky, M.; Xie, H.; Jiménez-Mier, J.; Liu, Y.-S.; Menéndez-Proupin, E.; Dunbar, K. R.; Lopez, N.; et al. Optical, Electronic, and Magnetic Engineering of ⟨111⟩ Layered Halide Perovskites. *Chem. Mater.* **2018**, *30* (15), 5315−5321.
(44) Tolbert, S. H.; Alivisatos, A. P. High-Pressure Structural Transformations in Semiconductor Nanocrystals. *Annu. Rev. Phys. Chem.* **1995**, *46* (1), 595−626.
(45) Wu, H.; Bai, F.; Sun, Z.; Haddad, R. E.; Boye, D. M.; Wang, Z.; Huang, J. Y.; Fan, H. Nanostructured Gold Architectures Formed through High Pressure-Driven Sintering of Spherical Nanoparticle Arrays. *J. Am. Chem. Soc.* **2010**, *132* (37), 12826−12828.
(46) Wang, Z.; Chen, O.; Cao, C. Y.; Finkelstein, K.; Smilgies, D.-M.; Lu, X.; Bassett, W. A. Integrating in situ high pressure small and wide angle synchrotron x-ray scattering for exploiting new physics of nanoparticle supercrystals. *Rev. Sci. Instrum.* **2010**, *81* (9), 093902.
(47) Yang, H.; Cai, T.; Dube, L.; Chen, O. Synthesis of double perovskite and quadruple perovskite nanocrystals through post-synthetic transformation reactions. *Chem. Sci.* **2022**, *13* (17), 4874−4883.
(48) Demirbilek, R.; Feile, R.; Çelik Bozdoğan, A. Temperature dependent Raman spectra of $CsCdBr_3$ and $CsCdCl_3$ crystals. *J. Lumin.* **2015**, *161*, 174−179.
(49) Meng, X.; Wei, Q.; Lin, W.; Huang, T.; Ge, S.; Yu, Z.; Zou, B. Efficient Yellow Self-Trapped Exciton Emission in Sb^{3+}-Doped $RbCdCl_3$ Metal Halides. *Inorg. Chem.* **2022**, *61* (18), 7143−7152.
(50) Nakashima, S.-i.; Yoshida, H.; Fukumoto, T.; Mitsuishi, A. Raman Spectra of $CdCl_2$, $CdBr_2$ and CdI_2. *J. Phys. Soc. Jpn.* **1971**, *31* (6), 1847−1847.
(51) Ma, Y.; Zhang, L.; Tang, Y.; Wu, S.; Tong, M.-L.; Wang, K.; Zou, B.; Li, M.-R. Pressure-Induced Piezochromism and Structure Transitions in Lead-Free Layered $Cs_4MnBi_2Cl_{12}$ Quadruple Perovskite. *ACS Appl. Energy Mater.* **2021**, *4*, 7513.
(52) Zhang, J.; Zheng, Y.; Liu, G.; Ma, Y.; Gong, L.; Guan, R.; Cui, X.; Yan, J.; Zhao, J.; Yang, J. Pressure-Engineered Optical and Charge Transport Properties of Mn^{2+}/Cu^{2+} Codoped $CsPbCl_3$ Perovskite Nanocrystals via Structural Progression. *ACS Appl. Mater. Interfaces* **2020**, *12* (42), 48225−48236.
(53) Wang, Z.; Schliehe, C.; Wang, T.; Nagaoka, Y.; Cao, Y. C.; Bassett, W. A.; Wu, H.; Fan, H.; Weller, H. Deviatoric Stress Driven Formation of Large Single-Crystal PbS Nanosheet from Nanoparticles and in Situ Monitoring of Oriented Attachment. *J. Am. Chem. Soc.* **2011**, *133* (37), 14484−14487.
(54) Li, Q.; Yin, L.; Chen, Z.; Deng, K.; Luo, S.; Zou, B.; Wang, Z.; Tang, J.; Quan, Z. High Pressure Structural and Optical Properties of Two-Dimensional Hybrid Halide Perovskite $(CH_3NH_3)_3Bi_2Br_9$. *Inorg. Chem.* **2019**, *58* (2), 1621−1626.

https://doi.org/10.1021/acs.jpcc.2c07970
J. Phys. Chem. C 2023, 127, 2407−2415

(55) Zhang, L.; Wang, L.; Wang, K.; Zou, B. Pressure-Induced Structural Evolution and Optical Properties of Metal-Halide Perovskite $CsPbCl_3$. *J. Phys. Chem. C* **2018**, *122* (27), 15220−15225.
(56) Cao, Y.; Qi, G.; Sui, L.; Shi, Y.; Geng, T.; Zhao, D.; Wang, K.; Yuan, K.; Wu, G.; Xiao, G.; et al. Pressure-Induced Emission Enhancements of Mn^{2+}-Doped Cesium Lead Chloride Perovskite Nanocrystals. *ACS Mater. Lett.* **2020**, *2* (4), 381−388.
(57) Zuo, T.; Sun, Z.; Zhao, Y.; Jiang, X.; Gao, X. The Big Red Shift of Photoluminescence of Mn Dopants in Strained CdS: A Case Study of Mn-Doped MnS-CdS Heteronanostructures. *J. Am. Chem. Soc.* **2010**, *132* (19), 6618−6619.

https://doi.org/10.1021/acs.jpcc.2c07970
J. Phys. Chem. C 2023, 127, 2407−2415